



# Femtosecond laser thinning for resistivity control of tungsten ditelluride thin-films synthesized from sol-gel deposited tungsten oxide

A. Fernández García<sup>a</sup>, M. Garcia-Lechuga<sup>b</sup>, F. Agulló Rueda<sup>c</sup>, J. Rubio Zuazo<sup>c,d</sup>,  
M. Manso Silvan<sup>a,\*</sup>

<sup>a</sup> Departamento de Física Aplicada, Centro de Microanálisis de Materiales and Instituto de Ciencia de Materiales Nicolás Cabrera, Universidad Autónoma de Madrid, Madrid, Spain

<sup>b</sup> Laser Processing Group, Instituto de Óptica "Daza de Valdés" (IO), CSIC, Madrid 28006, Spain

<sup>c</sup> Instituto de Ciencia de Materiales de Madrid (ICMM), CSIC, Madrid 28049, Spain

<sup>d</sup> SpLine, Spanish CRG BM25 Beamline at the ESRF, Grenoble F-38000, France

## ARTICLE INFO

### Keywords:

Transition metal dichalcogenides  
Tungsten ditelluride  
Sol-gel deposition  
Isothermal closed space vapor transport  
Fs laser processing

## ABSTRACT

In this work we present a route for fabricating WTe<sub>2</sub> thin-films together with femtosecond laser post processing, enabling to finely control the conductivity. First, we produce amorphous films of WO<sub>3</sub> on Si by spin-coating a sol-gel precursor followed by a consolidating annealing and a reduction process in partial H<sub>2</sub> atmosphere, leading to porous metallic tungsten cluster layers. To achieve WTe<sub>2</sub>, the films were exposed to the chalcogen vapours by isothermal closed space vapor transport. The formation of a tungsten ditelluride film composed of piled crystals could be confirmed and a gradient of surface rich Te identified through hard X-ray photoelectron spectroscopy. Finally, it is demonstrated that resistivity can be changed from 0.2 mΩ.m to 1 mΩ.m, while keeping the material characteristics. An anisotropic conductivity can be induced by direct selective thinning with fs laser writing (350 fs pulse duration, 515 nm laser wavelength) of 1D stripes. The obtained results, demonstrate that laser processing is a promising thin-film post-processing technique that can be applied to 2D transition metal dichalcogenide thin films.

## 1. Introduction

Monolayer and few-layered 2D materials are attracting a great attention recently due to their outstanding electronic properties, which give rise to a panorama of new applications in the fields of electronic [1, 2], optical [2,3], chemical [4,5,6] and biomedical [7,8] devices. Among the different families of 2D materials, transition metal dichalcogenides (TMDs) possess unique properties and have applications in various fields such as gas sensing, photocatalysis and energy storage devices [9,10, 11]. TMDs have the form MX<sub>2</sub>, where M is a transition metal and X is a chalcogen (S, Se, or Te) bound by strong covalent bonds in a 2D plane and forming layers bound by weak Van der Waals forces out of that plane. The versatility of properties of TMDs is partly due to their polymorphism, where metal coordination changes from distorted octahedral to trigonal [12]. For example, the well-studied MoS<sub>2</sub> is a semiconductor in its trigonal prismatic (2H) phase, which is the stable phase at room temperature. But when it shows up to the metastable octahedral (Td) phase, it presents a semi-metallic behaviour [13].

WTe<sub>2</sub> is one of the 2D materials belonging to the transition metal dichalcogenides family [14]. At ambient conditions, WTe<sub>2</sub> usually presents an orthorhombic (Td) phase [15]. This Td phase behaves as a semimetal [16] and has been found recently to have extremely high and no saturating magnetoresistance [17], as well as pressure-induced superconductivity [18]. Meanwhile, WTe<sub>2</sub> in its metastable trigonal prismatic (2H) phase is a semiconductor, and due to its bandgap and effective mass, is viewed as an integral part of the tunnel field effect transistor (TFET) [19].

One of the methods for obtaining large area few monolayer TMDs is the annealing of the transition metal (or the transition metal oxide) in the presence of vapours of a chalcogen element. So, sulfurization [20], selenization [21] and tellurization [22] have been frequently employed to prepare the corresponding TMDs. While WS<sub>2</sub> [23] and WSe<sub>2</sub> [24] have been obtained by this method, there are only a few reports of successful tellurization of tungsten [25,26].

In this paper, we report the preparation of WTe<sub>2</sub> by tellurization of previously deposited tungsten oxide films grown by sol-gel. We

\* Corresponding author.

E-mail address: [miguel.manso@uam.es](mailto:miguel.manso@uam.es) (M. Manso Silvan).

<https://doi.org/10.1016/j.surfin.2023.103668>

Received 30 July 2023; Received in revised form 10 November 2023; Accepted 22 November 2023

Available online 23 November 2023

2468-0230/© 2023 The Authors. Published by Elsevier B.V. This is an open access article under the CC BY-NC-ND license (<http://creativecommons.org/licenses/by-nc-nd/4.0/>).

performed isothermal close space (ICS) tellurization in a small volume and a semi-closed graphite crucible. In such a configuration, the Te vapor pressure approximately equals its equilibrium vapor pressure at the temperature of the annealing, and the Te source/substrate distance is very small. These characteristics favour the Te vapor transport and the efficiency of the tellurization [22,25].

Additionally, we present results on selectively controlling the resistivity of the  $\text{WTe}_2$  thin film after femtosecond laser irradiation. Femtosecond laser processing of thin films has been applied to a wide variety of materials, such as the technologically important silicon-on-insulator [27] or indium-tin oxide [28]. In most cases, micrometric modifications are achieved by generating laser-induced periodic surface structures (LIPSS) [29], which offers the advantage of enabling rapid patterning through self-organization processes without the need of strong focusing conditions (tens of micrometres spot sizes). This process requires the transformation and self-organization of the material, making the control of the induced transformation limited to the irradiation wavelength, the irradiation fluence and the material properties. However, direct laser writing is generally preferred to avoid material dependent transformations. The spatial resolution is controlled by the focusing conditions, making possible to reach high precision (micrometric or sub-micrometric scale) by strong focusing. As a drawback, the use of smaller spot sizes makes such processing slower. This strategy has been demonstrated to have strong potential for laser thinning of TMDs flakes (few layers) via precise control of their thickness (down to single layer) in materials such as  $\text{MoS}_2$  [30,31],  $\text{MoTe}_2$  [32,33] or  $\text{WS}_2$  [34]. As a drawback, this very precise strategy for the thinning of TMD flakes has been demonstrated useful only on very small areas.

Here, we show the possibility to precisely modify relatively large thin  $\text{WTe}_2$  thin-films via laser direct writing with femtosecond laser pulses (350-fs pulse duration), using visible radiation (515 nm wavelength) which allows higher spatial resolution than the most often used infrared radiation. The aim is to control the irradiation parameters, such as the micrometric control of the line-to-line separation (2 or 4  $\mu\text{m}$ ) or the fluence of irradiation (from the modification threshold and up to the full thin-film removal), to enable a tuning of the resistivity, and lead to an electrical anisotropy, without inducing chemical or thermal-related changes on the thin-film.

## 2. Experimental methods

### 2.1. Tungsten oxide film preparation

The  $\text{WO}_3$  precursor sol was prepared using tungsten (IV) chloride powder 95 % metal basis (Sigma Aldrich). A 0.8 M solution was

prepared with the tungsten chloride powder in ethanol. In parallel, a solution of ethanol, hydrochloric acid and water was prepared in a 0.001:1:0.005 vol ratio, respectively. Both were left to rest for 30 min. Then, they were mixed to obtain a final solution with a concentration of 0.39 M, like that of previous studies with  $\text{TiO}_2$  [35] and  $\text{MoO}_3$  [22].

A precursor droplet of 50  $\mu\text{L}$  was deposited onto (100) Si surface while spinning at 2000 rpm. The condensed films obtained were then annealed in open air for 10 min at 600 or 800  $^\circ\text{C}$ . The whole spin-coating/annealing process was repeated 3 times to produce thicker films. This first step is illustrated in the left part of Fig. 1a.

### 2.2. W and $\text{WTe}_2$ film preparation

The nucleated structures produced by sol-gel spin-coating were subsequently reduced at atmospheric pressure in  $\text{H}_2:\text{Ar}$  at 1:5 atmosphere at 600  $^\circ\text{C}$  for 1 h, which eventually allowed achieving W films.

For the isothermal closed space vapor (ICSV) tellurization, a graphite boat with a solid Te precursor was used. The sample annealed at 600  $^\circ\text{C}$  with a reducing gas mixture composed of  $\text{H}_2:\text{Ar}$  at 2:3 was exposed to the Te source for 15 min at atmospheric pressure [36]. The ICSV process is illustrated in the right part of Fig. 1a.

### 2.3. Film thinning by direct laser writing

The laser processing of the thin-films was carried out using a Satsuma HP2 Yb fiber laser from Amplitude Systems. The fundamental wavelength of the laser is 1030 nm with a pulse duration of 350 fs and emitting with a tuneable repetition rate between 1 and 500 kHz. Additionally, through a modulus for generating harmonics, 515 nm radiation is accessible. Since the objective of this work is to produce precise direct laser modification, the smaller spot size provided by this shorter wavelength motivates its use.

The laser power is attenuated with filters and fine controlled by the software of the laser system. The beam is focused to the sample by making use of a microscope objective (x20 NA 0.4), as sketched in Fig. 1 (b), having a Gaussian spot size diameter at the sample position of 3.1  $\mu\text{m}$  ( $1/e^2$ ). The sample is mounted on a motorized XYZ-axis platform (Aerotech) and perfectly aligned perpendicular to the laser beam. By moving the horizontal axis (X-axis) at a controlled speed of 10 mm/s and by setting the repetition rate at 50 kHz continuous and homogeneous modified lines are inscribed on the material. The laser peak fluence range is tested in processing the samples, finding that the optimum peak fluence to produce controlled thinning is between 85  $\text{mJ}/\text{cm}^2$  and 170  $\text{mJ}/\text{cm}^2$ . As a reference, under the same irradiation conditions amorphous lines in silicon were produced by using fluence values of 120  $\text{mJ}/\text{cm}^2$ .

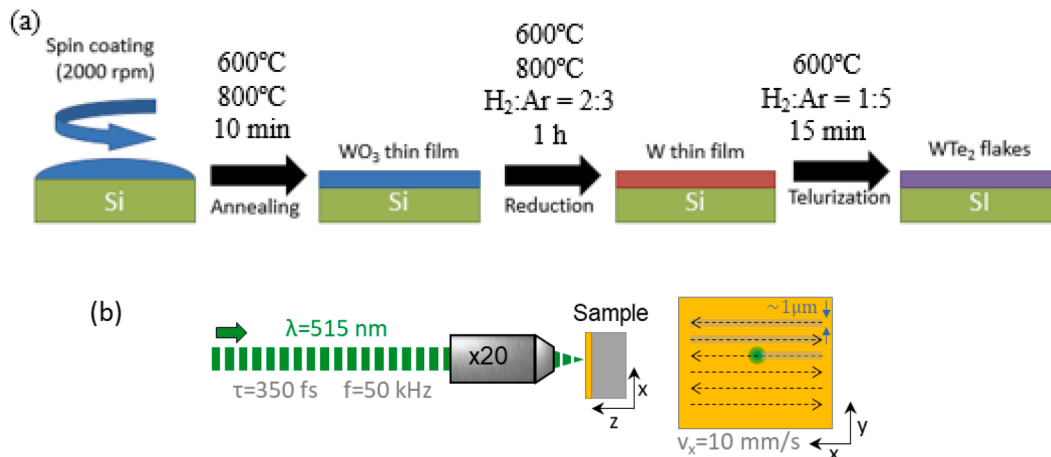


**Fig. 1.** (a) Preparation and synthesis of  $\text{WTe}_2$  films via reduction and tellurization of  $\text{WO}_3$  deposited by sol-gel spin-coating. (b) Sketch of the laser irradiation set-up (left) and the sample scanning strategy to fabricate modified 1D lines (right).

cm<sup>2</sup>. Areas of  $3.5 \times 3.0$  mm<sup>2</sup> are processed by writing horizontal lines and controlling the vertical line-to-line separation, exploring in this work separations of 2 and 4  $\mu$ m. To illustrate the speed of the process the machining time is 15 min. for the vertical separation of 2  $\mu$ m and 7 min. and 30 s for the separation of 4  $\mu$ m.

#### 2.4. Characterization

A morphological analysis was performed using a Field Emission Scanning Electron Microscope (FESEM) FEI VERIOS 4i and X-ray diffraction (XRD) with a Panalytical diffractometer X'Pert PRO ( $\Theta/2\Theta$  geometry, Cu anode and non-monochromatic ( $K_\alpha$ ) radiation). The synchrotron X-ray diffraction experiments were performed at BM25-B SpLine at the ESRF providing a wavelength of 0.8434 Å in a six-circle diffractometer in vertical geometry [37]. Raman spectra were obtained with a Renishaw Ramascope 2000 spectrometer and an Argon ion laser emitting at a wavelength of 514.5 nm. The laser power was maintained low to avoid sample damage. A metallographic optical microscope Olympus BH-2 was used to focus the laser light on the film and to collect the light scattered by the sample in a backscattering geometry. The optical axis was perpendicular to the sample surface. Hard X-ray photoelectron spectroscopy (HAXPES) measurements were performed at the BM-25 SpLine beamline of The European Synchrotron, Grenoble, France [38]. The experimental set-up includes a high electron kinetic energy analyser working from a few eV up to 15 keV [39]. All data were analysed using CasaXPS software after subtraction of a Shirley baseline, correcting charge shifts and determining chemical contribution through Gaussian/Lorentzian peak fitting. To measure the IV curve, four gold contacts have been circumscribed in the circular area of the sample and arranged in a gridded cross. The distance between the points of the cross is 2 mm so that they remain inside the irradiated area. A four-point

station with millimetric control of electrical contact positioning was used to interconnect with the IV acquisition system (Bio-Logic).

### 3. Results and discussion

The first step in the processing of the thin films was to analyse their growth process. For this we characterized the nucleation of the sol-gel tungsten oxide film by SEM. Fig. 2(a) and (b) shows the SEM images of the tungsten oxide samples. With an annealing temperature of 600°C we obtained a very porous thin film resembling a jelly paste. A cross section image (not shown) demonstrated a uniform thickness of 270 nm after only one spin-coating droplet. Whenever necessary, this thickness was increased by repeating the process. At 800 °C, the condensed film transforms. The formation of clusters, with a variety of geometric shapes and smooth edges is observed. Also, the size range is quite wide, from 100 to 300 nm. The appearance of these clusters is a phenomenon widely observed in WO<sub>3</sub> deposition processes involving a liquid phase precursor, such as in sol-gel [40].

The annealing performed in H<sub>2</sub> to induce reduction of the films was responsible of severe morphological transformations. The films reduced at 600 °C (Fig. 2c) still show the typical porous structure of the condensed WO<sub>x</sub> films, this time with a granular aspect. Furthermore, it is shown that the reducing process notably affects the evaporation of the WO<sub>x</sub> film, which justifies the cyclic deposition process of Fig. 1. This phenomenon is drastically accentuated at 800 °C (Fig. 2d) showing isolated island films containing again porous structures with smaller feature size with respect to that observed on the films reduced at 600 °C.

Then we studied the transformation induced by the annealing of the spin coated film and its reduction process by X-ray diffraction. Fig. 3(a) shows the diffractogram of the samples after the first condensation annealing. The phase that best corresponds to the experimental data, for

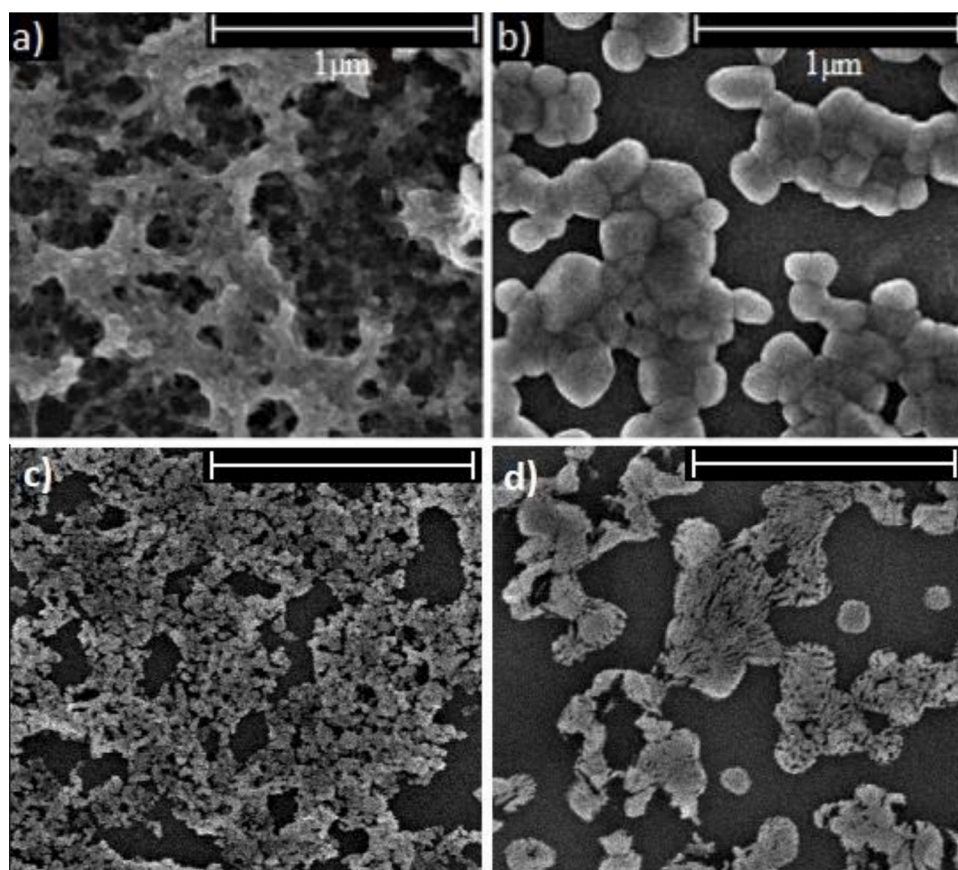


**Fig. 2.** (a) and (b) SEM images of tungsten oxide annealed at 600 and 800 °C, respectively. (c) and (d) SEM images of tungsten oxide films after reduction treatment at 600 and 800 °C, respectively.

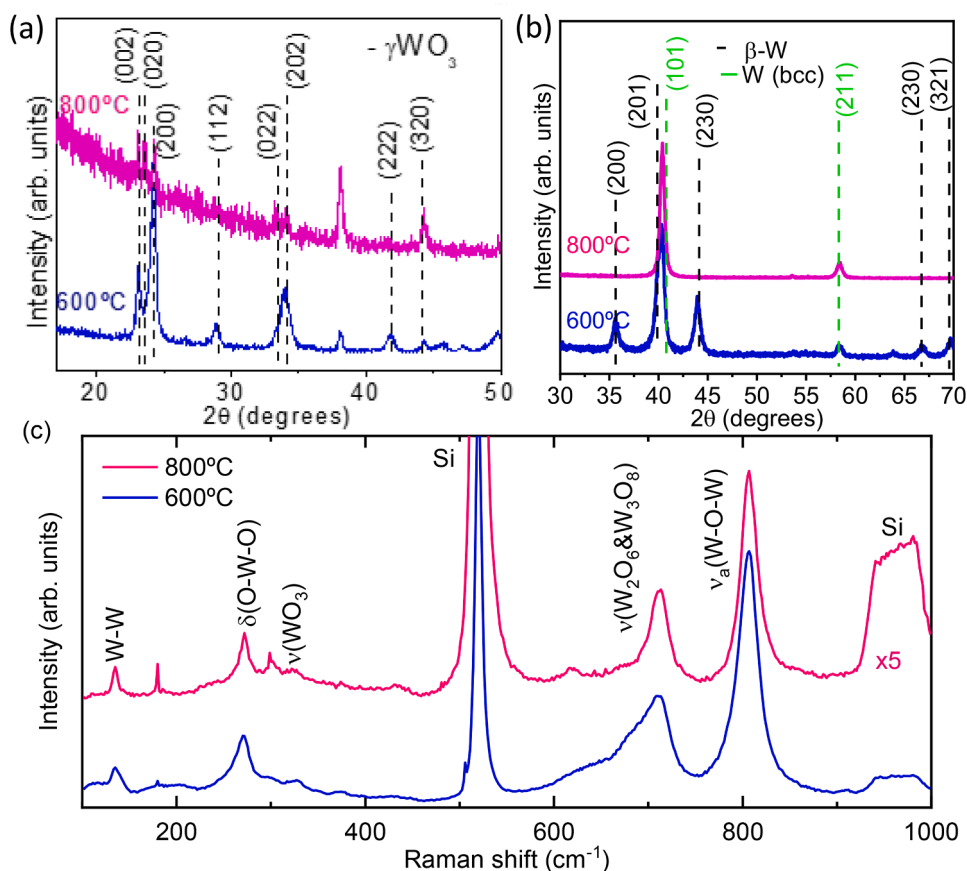


**Fig. 3.** (a) X-ray diffractogram of the tungsten oxide films annealed at 600 °C (bottom) and 800 °C (top). (b) X-ray diffractogram of the films reduced at 600 °C (bottom) and 800 °C (top). (c) Raman spectra of the tungsten oxide films annealed at 600 °C (bottom) and 800 °C (top).

both temperatures, is the monoclinic,  $\gamma\text{WO}_3$  (P1 21/n 1, COD 2,106,382) with unit cell parameters  $a = 7.306 \text{ \AA}$ ,  $b = 7.504 \text{ \AA}$  and  $c = 7.692 \text{ \AA}$ , which corresponds to the most stable  $\text{WO}_3$  phase [40,41]. All the peaks have been identified with this phase except the one that appears at  $2\theta \approx 38^\circ$ , which is due to the substrate [22]. The resolved (020) peak at  $2\theta \approx 23.51^\circ$  after annealing at 800 °C may be related to the previously described clusterization change observed by SEM, implying a growth of three-dimensional crystalline structures. A worsening of the signal to noise ratio and decrease in sample intensity (note relative increase of substrate related peak), is also observed in the sample annealed at 800 °C. This is related to the activated evaporation from  $\text{WO}_3$  clusters, leading to a non-conformal film compatible with what observed in the SEM image of Fig. 2b.

The X-ray diffractograms of the samples reduced by annealing in the presence of  $\text{H}_2$  are shown in Fig. 3(b). The peaks correspond to metallic W in its two crystalline phases: the metastable  $\beta\text{-W}$  (P m  $\bar{3}$  n, COD 9,008,583) [41–43] and the stable W-bcc (I m  $\bar{3}$  m, COD 9,011,611) [41]. Both are cubic with lattice parameter  $a = 5.083 \text{ \AA}$  and  $a = 3.158 \text{ \AA}$ , respectively. If the structure of  $\beta\text{-W}$  is a modification of the metallic tungsten or rather a suboxide, has been debated for a long time, but it seems more likely that it is a true modification of metallic tungsten [41]. The composition of the sample reduced at 600 °C obtained by Rietveld refinement was 56 %  $\beta\text{-W}$  phase and 44 % bcc W. Meanwhile, in the sample treated at 800 °C only W-bcc phase is present. Although it is not the main objective of this work, an additional method of growth for the two tungsten phases is presented. The synthesis of both W bcc as of  $\beta\text{-W}$  may be relevant for microelectronic and spintronic applications, respectively [42].

The nucleated tungsten oxide films were further characterized by Raman spectroscopy. Fig. 3(c) shows the Raman spectra of the  $\text{WO}_3$ ,

which presents mainly five vibrational bands centered at 805, 710, 320, 272 and  $135 \text{ cm}^{-1}$ . The peaks at 805, 710 and  $272 \text{ cm}^{-1}$  are typical modes of crystalline  $\text{WO}_3$  films. As has been reported in the literature the  $\text{WO}_3$  Raman bands sited in the range 750–950  $\text{cm}^{-1}$  are attributed to either the antisymmetric stretch of W-O-W bonds or the symmetric stretch of (O-W-O) bonds [44]. Most peaks below 200  $\text{cm}^{-1}$  are attributed to lattice vibrational modes, whereas the mid and high frequency regions correspond to deformation and stretching modes, respectively. Thus, the intense peaks centered at 805 and  $710 \text{ cm}^{-1}$  are typical Raman peaks of crystalline  $\text{WO}_3$  ( $\gamma$ -phase), which correspond to the stretching vibrations of the bridging oxygen [45,46] and these are assigned to O-W-O stretching ( $\nu$ ) modes [47,48]. The peaks at 272 and  $320 \text{ cm}^{-1}$  are assigned to the bending vibration  $\delta(\text{O-W-O})$  [47,49]. As in XRD, there is a decrease in the signal from the oxide, and, in addition for Raman, an increase in the signal from the silicon substrate when the annealing temperature is 800 °C. As seen in the SEM micrographs, it is patent that the material clumps and evaporates exposing the substrate.

Once the reduced samples were analysed, the one synthesized at 600 °C was selected for the conversion to  $\text{WTe}_2$  by means of ICSV tellurization. We chose the 600 °C annealed sample because it is formed by a continuous layer and not by non-conformal clusters as induced at 800 °C (see Fig. 2). After the tellurization, a significant change is observed in the morphology. The film changes from porous to a compact nanobrick film, as shown in Fig. 4(a) and (b). Also, the thickness of the tellurized samples increases, reaching 300 nm, due to the incorporation of Te in the structure, which increases the specific volume of the material [25].

$\text{WTe}_2$  exists in two crystalline phases with very different properties. The 2H (P6<sub>3</sub>/mmc) structure has semiconductor properties, while the Td (Pmn2<sub>1</sub>) is a semimetal [25,50]. In the diffractogram of Fig. 4(c) the characteristic peaks positions of both structures are superposed with the



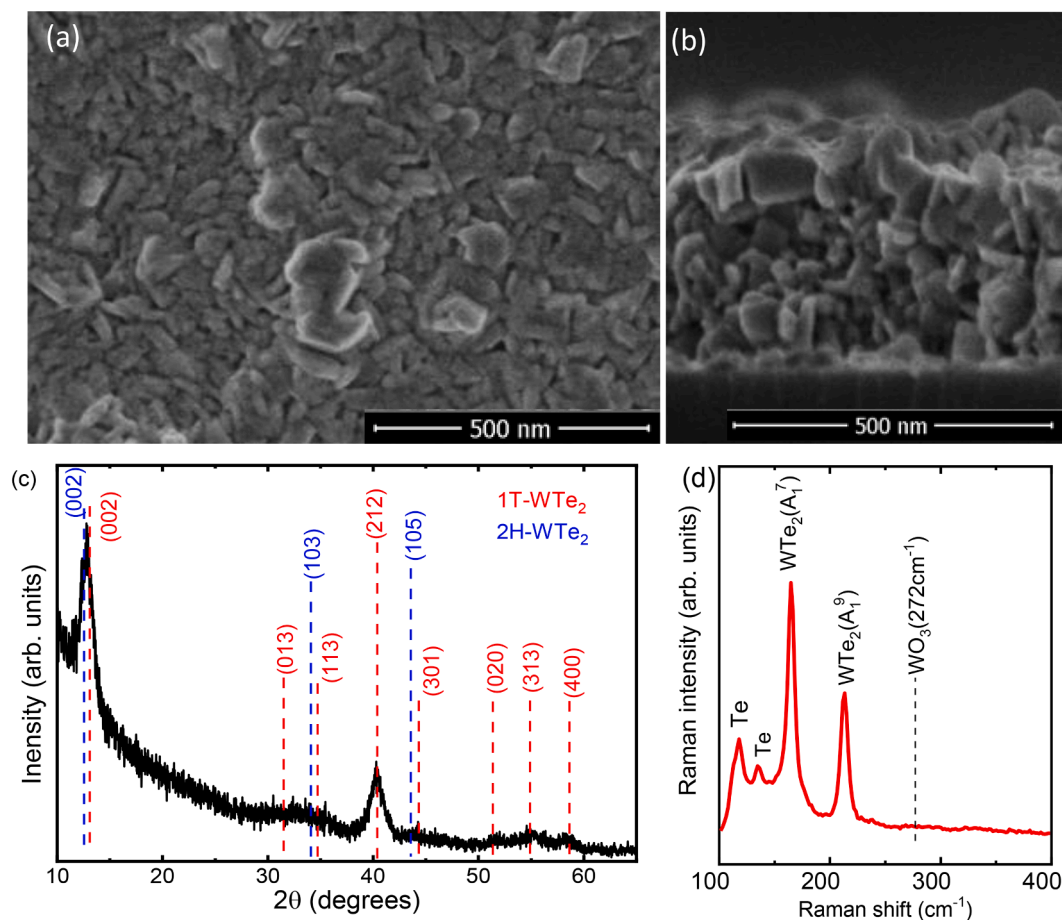


**Fig. 4.** (a) SEM micrograph from the surface and (b) cross-section of  $\text{WTe}_2$  film produced by Isothermal Closed Space Vapor transformation of the W film obtained at 600 °C. (c) X-ray diffractogram of the tellurized samples containing reference lines for the 1-Td and 2H crystal structures of  $\text{WTe}_2$ . (d) Raman spectrum of the tellurized films.

obtained experimental diffractogram. As can be seen, there is a contribution from both structures. Contrary to similar previous studies, there is no preferential growth of the  $\text{WTe}_2$  in the [001] direction [25]. A certain amount of excess Te cannot be discarded due to cooling post-tellurization [51], although the amount may be minimal and within

the background signal of the  $\text{WTe}_2$  phases. The Raman spectrum, Fig. 4 (d), confirms the presence of  $\text{WTe}_2$  and Te. The  $A_1'$  and  $A_1''$  modes have been named according to the notation in the literature [25,52]. There is no peak at 272  $\text{cm}^{-1}$  assigned to monoclinic  $\text{WO}_3$  [51], which indicates that almost all the tungsten in the films is successfully tellurized.

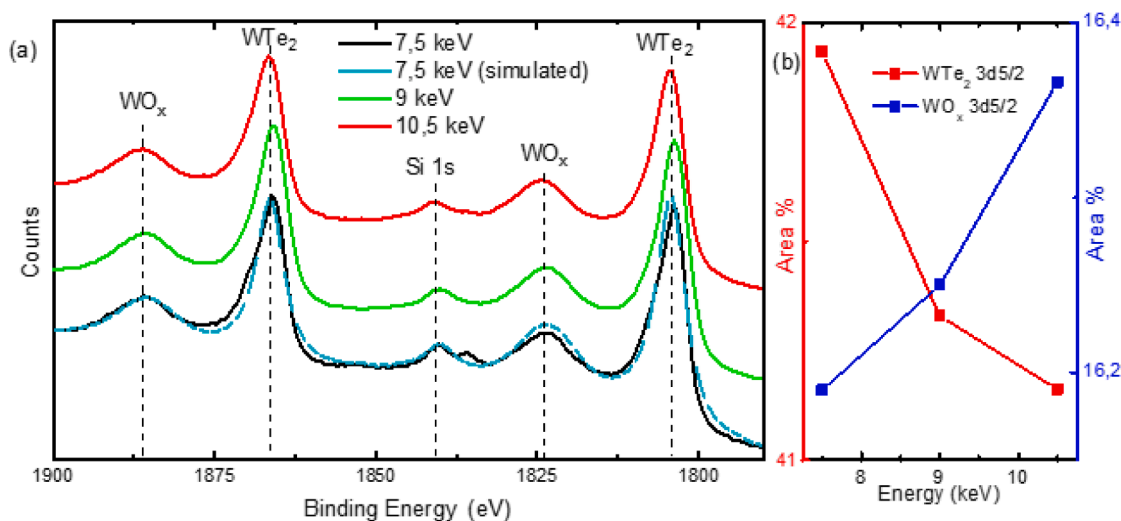


**Fig. 5.** (a) W 3d and Si 1s core level spectra acquired at three different X-ray energies (7.5; 9 and 10.5 keV) where two main W 3d contributions ( $\text{WTe}_2$  and  $\text{WO}_x$ ) can be distinguished. (b) Quantitative comparison of the concentration of  $\text{WTe}_2$  and  $\text{WO}_x$  as a function of the X-ray energy determined using the  $3d_{5/2}$  component.

HAXPES measurements were performed to characterize sample's composition in depth and determine if the tellurization process is superficial or proceeds smoothly to the substrate interface. Fig. 5(a) shows the HAXPES spectrum for the W 3d core level. Using three different X-ray energies we can study the chemical changes of this element that occur deeper in the film. The binding energy has been calibrated with the Si 1s peak at 1840 eV [53]. It is obtained that the highest intensity peaks have a binding energy (BE) of 2.7 eV above the BE of W 3d core level for the pure metal [54]. Several studies show that a BE displacement of less than 1 eV is expected for the W 3d core level of the W-Te bond [55,56]. Therefore, by comparison it can be deduced that the peaks obtained at BE of 1783 and 1845 eV (Fig. 5) correspond to the  $3d_{5/2}$  y  $3d_{3/2}$  core levels of  $WTe_2$ , respectively. The smaller peaks at 1823 and 1885 eV are due to a non-stoichiometric oxide since they are at a higher BE [55,56]. In Fig. 5(b) the relative area attributed to each bonding has been extracted at each X-ray excitation energy. This value is related to the amount of the said bonding in the sample. The intensity of the Si 1s increases as the energy of the photons does. On the one hand, the higher the energy of the X-ray beam, the higher the energy of the ejected electrons and therefore photoelectrons from deeper areas of substrate are detected. On the other hand, the relative area of the peaks attributed to  $WTe_2$  decreases with increasing energy, while those related to  $WO_x$  increase. These facts indicate that the tellurization occurs in depth and not only on the surface of the thin film. The fact that there is a higher proportion of  $WTe_2$  on the surface than in the bulk suggests that a Te diffusion process proceeds consistently during the final processing step of the  $WTe_2$  films. Thus, the thin film grown is not uniform in-depth and although the main component is the  $WTe_2$ , some  $WTe_{2x}O_{2(1-x)}$  ( $0 < x < 1$ ) can be predicted in depth thanks to the HAXPES study.

With the aim of controlling the resistivity and inducing electrical anisotropy in the thin film, inscription of horizontal lines with selective line-to-line separation has been made by direct laser writing. In particular, large micropatterned areas have been fabricated by using the following combinations: line spacing of 2  $\mu m$  and peak fluence of 170  $mJ/cm^2$ , spacing of 2  $\mu m$  and peak fluence of 85  $mJ/cm^2$  and spacing of 4  $\mu m$  and peak fluence of 170  $mJ/cm^2$ . Under the conditions of this later case, Fig. 6(a) shows the characteristics of the surface of the  $WTe_2$  thin-film after laser processing, demonstrating the high spatial resolution of

the laser inscription since the lines are clearly not overlapping. This is also confirmed for spacing of 2  $\mu m$ , as observed in the cross-section image in Fig. 6(b), where the modified regions are clearly separated by pristine areas. Additionally, this image also shows that for the higher fluence used (170  $mJ/cm^2$ ) the thin film is not fully ablated, and the written channels have approximately 1  $\mu m$  width. Irrespective of the width of the lines, both images show that there are transversal crossing imperfections in the laser generated lines as an effect of thin-film roughness.

Images in Fig. 6(c) and (d) show the composition map obtained by EDX before and after laser irradiation. In Fig. 6(d) is observed that in the regions modified by laser irradiation there is a decrease of W as well as of Te, indicating that the induced process involves material ablation of  $WTe_2$  and not selective ablation of one of the elements or a transformation into a composition richer in either W or Te. Therefore, it can be indirectly deduced that the laser only generates thinning, since the signal of none of the compounds disappears. Additionally, we can also deduce that oxidation is not produced, since the signal of Te does not decrease significantly with respect to the one of W, as expected in case of oxidation.

Placing four cross-shaped electrical gold contacts, the electrical resistivity has been measured in a perpendicular and parallel direction to the lines generated by laser writing. No metal-semiconductor junction behavior has been observed in the IV curves. This is important because it allows confirming that no oxidation of  $WTe_2$  is induced; since  $WO_3$  is a semiconductor and  $WTe_2$  is mostly identified in the Td semimetal phase in our films [57]. This reinforces the hypothesis that selective laser thinning does not induce total ablation, nor drastic oxidation, supporting the above mentioned EDX concentration maps. The resistivity values obtained from the experiment are shown in Fig. 7 and are in agreement with the expected laser thinning effect. An increase of the resistivity is observed with respect to the as-synthesized material. The resistivity values obtained are within the order of magnitude for Td- $WTe_2$  in bulk form [14], which suggests a dominant electrical transport effect through this phase in agreement with the dominant phase identified by Rietveld refinement. Regarding these results, there are two main observations of applicative interest: (a) a notorious resistance anisotropy and (b), the possibility to finely tune resistivity values. The observed resistance

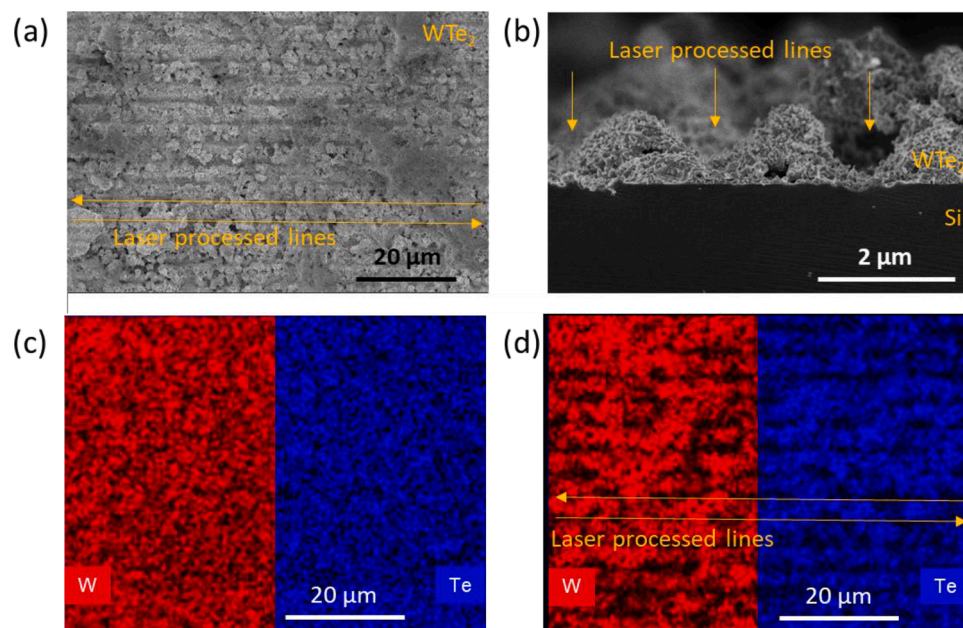


**Fig. 6.** (a) SEM micrograph of a selectively laser thinned region with 4  $\mu m$  line separation obtained at a peak fluence of 170  $mJ/cm^2$ . (b) SEM image of a cleaved sample of a selectively laser thinned region with 2  $\mu m$  line separation obtained at a peak fluence of 170  $mJ/cm^2$ . (c) and (d) Composition maps obtained by EDX for W and Te: (c) for the as grown thin-film and (d) after thinning by laser irradiation with 4  $\mu m$  line separation at a peak fluence of 170  $mJ/cm^2$ .

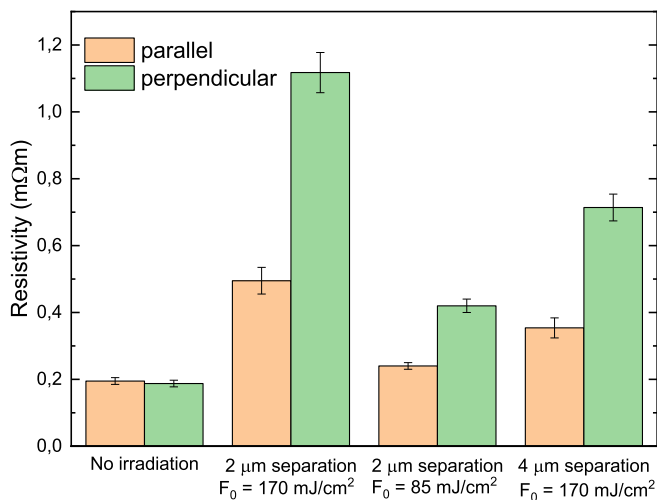


**Fig. 7.** Comparison of the resistivity between the perpendicular and parallel directions, with respect to the direct laser writing conditions: line spacing and laser peak fluence. The rest of the direct laser writing parameters are kept the same: sample speed of 10 mm/s and laser repetition rate of 50 kHz.

anisotropy is originated by the geometry of the laser irradiation induced modifications. The conductivity in an axis perpendicular to the line direction is decreased since electrons find periodic abrupt changes on the thickness along its propagation. A quantitative analysis of this induced anisotropy indicates resistivity values larger for the perpendicular direction with respect to the parallel one, reaching a factor close to 2 for all the tested irradiation conditions. Regarding the tuning of resistivity values, this is achieved by either the laser fluence or by the line-to-line separation. First, varying the laser fluence, which enables to control the quantity of removed material, demonstrates that the higher the fluence ( $170 \text{ mJ/cm}^2$ ), the higher the increase of resistivity. Secondly, the same logic applies when comparing surface processed with less or more line separation. As the density of lines decreases (greater separation) the change is less significant because the total surface modified is smaller.

These results confirm the advantages of laser thinning over other techniques such as mechanical exfoliation. An absolute error of less than 50 nm in thinning is estimated to be the maximum accuracy achievable under the presented conditions. This value was estimated on the following basis. First, by observing the optical properties of this material [58], it is assumed that laser absorption is triggered by linear absorption, rather than via multiphoton absorption, which results in ablated profiles being more abrupt and strongly dependent on the laser intensity [59]. Second, the modification process is performed in multishot conditions, leading to a larger ablation depth compared to single-shot conditions. However, even if multipulse irradiation poses a drawback to thinning accuracy, the relatively low number of pulses used in these conditions tends to keep this accuracy realistically below 50 nm in depth (following the formula  $N_{\text{eff}} = d_{\text{eff}} f_{\text{rep}} / v_{\text{scan}}$  given in [60], a total of 7 effective pulses is obtained). Therefore, there is a great precision in the control of the amount of material that is removed (control of the final thickness), which is crucial for the properties of 2D materials structures, and in particular, thin films. In addition, with this technique a spatial control of the slackening process is achieved, which allows the generation of structures with great precision or, as in this case, inducing fine tuning of electrical anisotropic properties.

#### 4. Conclusions

This work introduces a synthesis route to obtain thin films of  $\text{WTe}_2$ . First, using the sol-gel technique, a condensation annealing, and a thermally activated reduction at  $600^\circ\text{C}$  in a partial  $\text{H}_2$  atmosphere, precursor metallic W films are obtained. Moderate processing

temperatures of  $600^\circ\text{C}$  are selected as a compromise between the desired polycrystalline film formation and mitigated film evaporation with respect to higher annealing temperatures. With the subsequent isothermal closed space vapor tellurization of these films at identical temperature, it is possible to obtain 300 nm thick coatings of  $\text{WTe}_2$  presenting a nanobrick microstructure. The presence of  $\text{WTe}_2$  is confirmed by X-ray diffraction and Raman spectroscopy. An in-depth study of the resulting film after tellurization with hard X-ray photoelectron spectroscopy confirms that the 300 nm thick film is mainly composed of  $\text{WTe}_2$ , with an increasing O content at the interface with the substrate but preserving a  $\text{WTe}_{2x}\text{O}_{2(1-x)}$  stoichiometry, with x remaining close to one as suggested by the Raman and XRD analyses.

In addition, by selective and precise thinning by femtosecond direct laser writing, it has been demonstrated the final tuning of the resistivity of  $\text{WTe}_2$  as well as the possibility to easily induce electrical anisotropies. These anisotropies are conceived as potential sources for gas sensing.

#### Declaration of Competing Interest

The authors declare that they have no known competing financial interests or personal relationships that could have appeared to influence the work reported in this paper.

#### Acknowledgments

The current research was funded through grants PID2020-112770RB-C21 and PID2020-112770RB-C22 by MCIN/AEI/10.13039/501100011033. We acknowledge the Spanish MCIN and CSIC for provision of synchrotron radiation at the Spanish line at the ESRF trough project 25-02-972. We acknowledge the service from the MiNa Laboratory at IMN, and funding from CM (project S2018/NMT-4291 TEC2SPACE), MINECO (project CSIC13-4E-1794) and EU (FEDER, FSE).

#### References

- [1] Q. Zhao, Z. Xie, Y.P. Peng, K. Wang, H. Wang, X. Li, H. Wang, J. Chen, H. Zhang, X. Yan, Current status and prospects of memristors based on novel 2D materials, *Mater. Horiz.* 7 (2020) 1495–1518.
- [2] F. Li, T. Shen, C. Wang, Y. Zhang, J. Qi, H. Zhang, Recent advances in strain-induced piezoelectric and piezoresistive effect-engineered 2D semiconductors for adaptive electronics and optoelectronics, *Nano Micro Lett.* 12 (2020) 1–44.
- [3] B. Wang, S. Zhong, Y. Ge, H. Wang, X. Luo, H. Zhang, Present advances and perspectives of broadband photo-detectors based on emerging 2D-Xenes beyond graphene, *Nano Res.* 13 (2020) 891–918.
- [4] D. Zhang, Z. Yang, S. Yu, Q. Mi, Q. Pan, Diversiform metal oxide-based hybrid nanostructures for gas sensing with versatile prospects, *Coord. Chem. Rev.* 413 (2020), 213272.
- [5] S. Yuan, S.Y. Pang, J. Hao, 2D transition metal dichalcogenides, carbides, nitrides, and their applications in supercapacitors and electrocatalytic hydrogen evolution reaction, *Appl. Phys. Rev.* 7 (2020), 021304.
- [6] R.K. Jha, N. Bhat, Recent progress in chemiresistive gas sensing technology based on molybdenum and tungsten chalcogenide nanostructures, *Adv. Mater. Interfaces* 7 (2020), 1901992.
- [7] B. Ren, Y. Wang, J.Z. Ou, Engineering two-dimensional metal oxides via surface functionalization for biological applications, *J. Mater. Chem. B* 8 (2020) 1108–1127.
- [8] G.P. Neupane, L. Zhang, T. Yildirim, K. Zhou, B. Wang, Y. Tang, W. Ma, Y. Xue, Y. Lu, A prospective future towards bio/medical technology and bioelectronics based on 2D vdWs heterostructures, *Nano Res.* 13 (2020) 1–17.
- [9] S. Jo, N. Ubrig, H. Berger, A.B. Kuzmenko, A.F. Morpurgo, Mono-and bilayer  $\text{WS}_2$  light-emitting transistors, *Nano Lett.* 14 (2014) 2019–2025.
- [10] H. Li, Y. Cui, T. Wang, H. Luo, The band alignments modulation of g-MoTe<sub>2</sub>/WTe<sub>2</sub> van der Waals heterostructures, *Appl. Phys. A* 125 (2019) 1–10.
- [11] Q.H. Wang, K. Kalantar-Zadeh, A. Kis, J.N. Coleman, M.S. Strano, Electronics and optoelectronics of two-dimensional transition metal dichalcogenides, *Nat. Nanotechnol.* 7 (2012) 699–712.
- [12] H. Lv, W. Lu, D. Shao, Y. Liu, S. Tan, Y. Sun, Perfect charge compensation in WTe<sub>2</sub> for the extraordinary magnetoresistance: from bulk to monolayer, *Europhys. Lett.* 110 (2015) 37004.
- [13] R. Kappera, D. Voiry, S.E. Yalcin, B. Branch, G. Gupta, A.D. Mohite, M. Chhowalla, Phase-engineered low-resistance contacts for ultrathin MoS<sub>2</sub> transistors, *Nat. Mater.* 13 (2014) 1128–1134.



- [14] C.H. Lee, E.C. Silva, L. Calderin, M.A.T. Nguyen, M.J. Hollander, B. Bersch, T. E. Mallouk, J.A. Robinson, Tungsten ditelluride: a layered semimetal, *Sci. Rep.* 5 (2015) 10013.
- [15] J.M. Woods, D. Hynek, P. Liu, M. Li, J.J. Cha, Synthesis of WTe<sub>2</sub> nanowires with increased electron scattering, *ACS Nano* 13 (2019) 6455–6460.
- [16] J. Augustin, V. Eyert, T. Böker, W. Frentrup, H. Dwelk, C. Janowitz, R. Mancke, Electronic band structure of the layered compound Td–WTe<sub>2</sub>, *Phys. Rev. B* 62 (2000) 10812.
- [17] M.N. Ali, J. Xiong, S. Flynn, J. Tao, Q.D. Gibson, L.M. Schoop, T. Liang, N. Haldolaarachchige, M. Hirschberger, N.P. Ong, Large, non-saturating magnetoresistance in WTe<sub>2</sub>, *Nature* 514 (2014) 205–208.
- [18] X.C. Pan, X. Chen, H. Liu, Y. Feng, Z. Wei, Y. Zhou, Z. Chi, L. Pi, F. Yen, F. Song, Pressure-driven dome-shaped superconductivity and electronic structural evolution in tungsten ditelluride, *Nat. Commun.* 6 (2015) 7805.
- [19] H. Ilatikhameneh, Y. Tan, B. Novakovic, G. Klimeck, R. Rahman, J. Appenzeller, Tunnel field-effect transistors in 2-D transition metal dichalcogenide materials, *IEEE J. Explor. Solid State Comput. Devices Circuits* 1 (2015) 12–18.
- [20] Y. Zhan, Z. Liu, S. Najmaei, P.M. Ajayan, J. Lou, Large-area vapor-phase growth and characterization of MoS<sub>2</sub> atomic layers on a SiO<sub>2</sub> substrate, *Small* 8 (2012) 966–971.
- [21] Y. Wang, L. Li, W. Yao, S. Song, J. Sun, J. Pan, X. Ren, C. Li, E. Okunishi, Y. Q. Wang, Monolayer PtSe<sub>2</sub>, a new semiconducting transition-metal-dichalcogenide, epitaxially grown by direct selenization of Pt, *Nano Lett.* 15 (2015) 4013–4018.
- [22] A. Garcia, V. Torres-Costa, O. de Melo, F. Agullo-Rueda, G. Castro, M. Silvan, Growth of out-of-plane standing MoTe<sub>2</sub>(1-x)Se<sub>2x</sub>/MoSe<sub>2</sub> composite flake films by sol-gel nucleation of MoO<sub>y</sub> and isothermal closed space telluro-selenization, *Appl. Surf. Sci.* (2021) 546.
- [23] A.L. Elías, N. Perea-López, A. Castro-Beltrán, A. Berkdemir, R. Lv, S. Feng, A. D. Long, T. Hayashi, Y.A. Kim, M. Endo, Controlled synthesis and transfer of large-area WS<sub>2</sub> sheets: from single layer to few layers, *ACS Nano* 7 (2013) 5235–5242.
- [24] J.K. Huang, J. Pu, C.L. Hsu, M.H. Chiu, Z.Y. Juang, Y.H. Chang, W.H. Chang, Y. Iwasa, T. Takenobu, L.J. Li, Large-area synthesis of highly crystalline WSe<sub>2</sub> monolayers and device applications, *ACS Nano* 8 (2014) 923–930.
- [25] O. de Melo, M. Sanchez, A. Borroto, C. de Melo, B. Garcia, J. Pau, D. Horwat, WTe<sub>2</sub> synthesis by tellurization of W precursors using isothermal close space vapor transport annealing, *Phys. Status Solidi A Appl. Mater. Sci.* 215 (2018) 1800425.
- [26] M. Gao, M. Zhang, W. Niu, Y. Chen, M. Gu, H. Wang, F. Song, P. Wang, S. Yan, F. Wang, Tuning the transport behavior of centimeter-scale WTe<sub>2</sub> ultrathin films fabricated by pulsed laser deposition, *Appl. Phys. Lett.* 111 (2017), 031906.
- [27] J. Huang, L. Jiang, X. Li, S. Zhou, S. Gao, P. Li, L. Huang, K. Wang, L. Qu, Controllable photonic structures on silicon-on-insulator devices fabricated using femtosecond laser lithography, *ACS Appl. Mater. Interfaces* 13 (2021) 43622–43631.
- [28] C. Lopez-Santos, D. Puerto, J. Siegel, M. Macias-Montero, C. Florian, J. Gil-Rostra, V. López-Flores, A. Borras, A.R. González-Elipé, J. Solís, Anisotropic resistivity surfaces produced in ITO films by laser-induced nanoscale self-organization, *Adv. Opt. Mater.* 9 (2021), 2001086.
- [29] J. Bonse, S. Höhm, S.V. Kirner, A. Rosenfeld, J. Krüger, Laser-induced periodic surface structures—A scientific evergreen, *IEEE J. Sel. Top. Quantum Electron.* 23 (2016) 9000615.
- [30] A. Castellanos-Gomez, M. Barkelid, A. Goossens, V.E. Calado, H.S. van der Zant, G. A. Steele, Laser-thinning of MoS<sub>2</sub>: on demand generation of a single-layer semiconductor, *Nano Lett.* 12 (2012) 3187–3192.
- [31] Y. Rho, J. Pei, L. Wang, Z. Su, M. Eliceiri, C.P. Grigoropoulos, Site-selective atomic layer precision thinning of MoS<sub>2</sub> via laser-assisted anisotropic chemical etching, *ACS Appl. Mater. Interfaces* 11 (2019) 39385–39393.
- [32] V.K. Nagareddy, T.J. Octon, N.J. Townsend, S. Russo, M.F. Craciun, C.D. Wright, Humidity-controlled ultralow power layer-by-layer thinning, nanopatterning and bandgap engineering of MoTe<sub>2</sub>, *Adv. Funct. Mater.* 28 (2018), 1804434.
- [33] S. Kang, D. Won, H. Yang, C.H. Lin, C.S. Ku, C.Y. Chiang, S. Kim, S. Cho, Phase-controllable laser thinning in MoTe<sub>2</sub>, *Appl. Surf. Sci.* 563 (2021), 150282.
- [34] A. Venkatakrishnan, H. Chua, P. Tan, Z. Hu, H. Liu, Y. Liu, A. Carvalho, J. Lu, C. H. Sow, Microsteganography on WS<sub>2</sub> monolayers tailored by direct laser painting, *ACS Nano* 11 (2017) 713–720.
- [35] M. Langlet, M. Burgos, C. Coutier, C. Jimenez, C. Morant, M. Manso, Low temperature preparation of high refractive index and mechanically resistant sol-gel TiO<sub>2</sub> films for multilayer antireflective coating applications, *J. Solgel Sci. Technol.* 22 (2001) 139–150.
- [36] O. de Melo, L. Garcia-Pelayo, Y. Gonzalez, O. Concepcion, M. Manso-Silvan, R. Lopez-Nebreda, J. Pau, J. Gonzalez, A. Climent-Font, V. Torres-Costa, Chemically driven isothermal closed space vapor transport of MoO<sub>2</sub>: thin films, flakes and *in situ* tellurization, *J. Mater. Chem. C* 6 (2018) 6799–6807.
- [37] J. Rubio-Zuazo, P. Ferrer, A. López, A. Gutiérrez-León, I. Da Silva, G. Castro, The multipurpose X-ray diffraction end-station of the BM25B-SpLine synchrotron beamline at the ESRF, nuclear instruments and methods in, *Phys. Res. A Accel. Spectrom. Detect. Assoc. Equip.* 716 (2013) 23–28.
- [38] J. Rubio-Zuazo, G. Castro, Hard X-ray photoelectron spectroscopy (HAXPES)(≤15keV) at SpLine, the Spanish CRG beamline at the ESRF, nuclear instruments and methods in, *Phys. Res. A Accel. Spectrom. Detect. Assoc. Equip.* 547 (2005) 64–72.
- [39] J. Rubio-Zuazo, M. Escher, M. Merkel, G. Castro, High voltage-cylinder sector analyzer 300/15: a cylindrical sector analyzer for electron kinetic energies up to 15keV, *Rev. Sci. Instrum.* 81 (2010), 043304.
- [40] H. Zheng, J. Ou, M. Strano, R. Kaner, A. Mitchell, K. Kalantar-Zadeh, Nanostructured tungsten oxide - properties, synthesis, and applications, *Adv. Funct. Mater.* 21 (2011) 2175–2196.
- [41] H.J. Lunk, H. Hartl, Discovery, properties and applications of tungsten and its inorganic compounds, *ChemTexts* 5 (2019) 15.
- [42] K. Barmak, J. Liu, L. Harlan, P. Xiao, J. Duncan, G. Henkelman, Transformation of topologically close-packed beta-W to body-centered cubic alpha-W: comparison of experiments and computations, *J. Chem. Phys.* 147 (2017) 152709.
- [43] M. Baba, K.O.K. Ohta, T.I.T. Ikeda, Preparation of metallic W film by H<sub>2</sub>-reduction of WO<sub>3</sub> electron-resist film, *Jpn. J. Appl. Phys.* 30 (1991) 2581.
- [44] M. Daniel, B. Desbat, J. Lassegues, R. Garie, Infrared and Raman spectroscopies of rf sputtered tungsten oxide films, *J. Solid State Chem.* 73 (1988) 127–139.
- [45] P. Tägtström, U. Jansson, Chemical vapour deposition of epitaxial WO<sub>3</sub> films, *Thin Solid Films* 352 (1999) 107–113.
- [46] G. De Wijs, R. De Groot, Amorphous WO<sub>3</sub>: a first-principles approach, *Electrochim. Acta* 46 (2001) 1989–1993.
- [47] M. Daniel, B. Desbat, J. Lassegues, B. Gerand, M. Figlarz, Infrared and Raman study of WO<sub>3</sub> tungsten trioxides and WO<sub>3</sub>·xH<sub>2</sub>O tungsten trioxide hydrates, *J. Solid State Chem.* 67 (1987) 235–247.
- [48] E. Salje, Lattice dynamics of WO<sub>3</sub>, *Acta Crystallogr. A Cryst. Phys. Diff. Theor. Gen. Crystallogr.* 31 (1975) 360–363.
- [49] A. Rougier, F. Portemer, A. Quedé, M. El Marssi, Characterization of pulsed laser deposited WO<sub>3</sub> thin films for electrochromic devices, *Appl. Surf. Sci.* 153 (1999) 1–9.
- [50] S. Li, F.C. Lei, X. Peng, R.Q. Wang, J.F. Xie, Y.P. Wu, D.S. Li, Synthesis of semiconducting 2H-phase WTe<sub>2</sub> nanosheets with large positive magnetoresistance, *Inorg. Chem.* 59 (2020) 11935–11939.
- [51] T. Caruso, M. Castriota, A. Pollicicchio, A. Fasanella, M. De Santo, F. Ciuchi, G. Desiderio, S. La Rosa, P. Rudolf, R. Agostino, E. Cazzanelli, Thermally induced evolution of sol-gel grown WO<sub>3</sub> films on ITO/glass substrates, *Appl. Surf. Sci.* 297 (2014) 195–204.
- [52] Y. Kim, Y.I. Jhon, J. Park, J.H. Kim, S. Lee, Y.M. Jhon, Anomalous Raman scattering and lattice dynamics in mono-and few-layer WTe<sub>2</sub>, *Nanoscale* 8 (2016) 2309–2316.
- [53] M. Klasson, A. Berndtsson, J. Hedman, R. Nilsson, R. Nyholm, C. Nordling, Electron escape depth in silicon, *J. Electron Spectrosc. Relat. Phenom.* 3 (1974) 427–434.
- [54] W. Huschka, D. Ross, M. Maier, E. Umbach, Calibrated binding energies of some core levels in the energy range between 1.5–4keV, *J. Electron Spectrosc. Relat. Phenom.* 46 (1988) 273–276.
- [55] M. Cao, Z. Wang, L. Ma, L. Zhang, M. Wang, Y. Liu, J. He, X. Xi, Tungsten ditelluride: synthesis, structure, and magnetoresistance property, *Adv. Electron. Mater.* 7 (2021), 2000893.
- [56] L.A. Walsh, R. Yue, Q. Wang, A.T. Barton, R. Addou, C.M. Smyth, H. Zhu, J. Kim, L. Colombo, M.J. Kim, WTe<sub>2</sub> thin films grown by beam-interrupted molecular beam epitaxy, *2D Mater.* 4 (2017), 025044.
- [57] O. de Melo, F. Agulló-Rueda, V. Torres-Costa, Spatially resolved MoO<sub>x</sub> phases by the laser oxidation of MoO<sub>2</sub>: a possible route for all-molybdenum oxide devices, *J. Mater. Chem. C* 9 (2021) 6579–6588.
- [58] B. Munkhbat, P. Wróbel, T.J. Antosiewicz, T.O. Shegai, Optical constants of several multilayer transition metal dichalcogenides measured by spectroscopic ellipsometry in the 300–1700nm range: high index, anisotropy, and hyperbolicity, *ACS Photon.* 9 (2022) 2398–2407.
- [59] J. Byskov-Nielsen, J.M. Savolainen, M.S. Christensen, P. Balling, Ultra-short pulse laser ablation of metals: threshold fluence, incubation coefficient and ablation rates, *Appl. Phys. A* 101 (2010) 97–101.
- [60] D. Puerto, M. García-Lechuga, J. Hernandez-Rueda, A. Garcia-Leis, S. Sanchez-Cortes, J. Solís, J. Siegel, Femtosecond laser-controlled self-assembly of amorphous-crystalline nanogratings in silicon, *Nanotechnology* 27 (2016), 265602.